

Effects of Ti additions on the nanostructure and creep properties of precipitation-strengthened Al–Sc alloys

Marsha E. van Dalen ^{*}, David C. Dunand, David N. Seidman

Department of Materials Science and Engineering, Northwestern University, 2220 Campus Dr., Evanston, IL 60208-3108, USA

Received 31 March 2005; received in revised form 16 May 2005; accepted 16 May 2005

Available online 5 July 2005

Abstract

Three-dimensional atom-probe tomography, transmission electron microscopy and microhardness were used to investigate the temporal evolution of nanosize, coherent $\text{Al}_3(\text{Sc}_{1-x}\text{Ti}_x)$ precipitates (L1_2 structure) in a coarse-grained Al–0.06at.%Sc–0.06at.%Ti alloy aged between 300 and 450 °C. At 300 °C, most scandium atoms partition within one day to the precipitates, whereas titanium atoms, even after 64 days of aging, remain predominantly in solid solution in the matrix, resulting in precipitates with average composition $\text{Al}_3(\text{Sc}_{0.94}\text{Ti}_{0.06})$. While titanium is very effective at retarding the coarsening kinetics of the precipitates, the low levels of titanium substitution result in only modest hardness increases over the binary Al–0.06at.%Sc alloy. When crept at 300 °C, the peak-aged alloy exhibits a threshold stress, which when normalized by the Orowan stress, increases with increasing radius, as predicted by a recent model considering elastic interactions between dislocations and coherent precipitates, and as previously observed in Al–Sc–Zr alloys.

© 2005 Acta Materialia Inc. Published by Elsevier Ltd. All rights reserved.

Keywords: Aluminum alloys; Precipitation; Coarsening; Three-dimensional atom-probe tomography; Creep

1. Introduction

Small additions of scandium to aluminum, within the maximum solubility of 0.23 at.% (0.38 wt.%) at the eutectic temperature, lead to the formation of nanosize, Al_3Sc precipitates with the L1_2 structure, which form homogeneously during aging from a single-phase supersaturated solid-solution [1–3]. Due to the lattice parameter misfit between the Al_3Sc precipitates and the α -Al matrix, ($\delta = 1.10\%$ at 300 °C [4]) and the resulting lattice strains, the precipitates remain coherent to diameters of about 40 nm [5,6]. These dilute Al–Sc alloys provide high strength at ambient temperature by both precipitation and grain boundary strengthening [7], the latter effect resulting from stabilization of a very fine grain structure by Al_3Sc precipitates for hypereutectic alloys

[8]. At elevated temperature, the high stability and coarsening resistance of the precipitates maintain this fine grain structure, leading to superplastic behavior [9]. If, however, the alloy is homogenized at high homologous temperatures in the single-phase α -Al region, a coarse-grained matrix forms. After peak aging, these coarse-grained alloys display high creep resistance, as demonstrated in previous articles on Al–Sc alloys [10–13]. The formation of a high number density of coherent, nanosize Al_3Sc precipitates was found to be a very efficient obstacle to dislocation climb, resulting in a threshold stress behavior at 300 °C and creep resistance better than any other known castable, heat-treatable aluminum alloy.

To further improve the creep properties of coarse-grained Al–Sc alloys, the effects of ternary additions have been investigated. Magnesium additions lead to solid-solution strengthening of the α -Al matrix [13]. For creep at high strain rates, solid-solution strengthening

^{*} Corresponding author. Tel.: +1 847 491 5946.

E-mail address: vandalen@northwestern.edu (M.E. van Dalen).

is additive to precipitation strengthening. Yet, Mg does not significantly alter the near-threshold creep behavior at low strain rates [13]. Zirconium additions to Al–Sc alloys have also been studied, as Zr partitions to the Al_3Sc precipitates [14]. In the bulk intermetallic $\text{Al}_3(\text{Sc},\text{Zr})$ phase, Zr can replace up to half of the Sc while retaining the L_{12} structure [4,8]. Since Zr has a much lower cost than Sc, the same precipitate volume fraction could be retained while employing a smaller amount of Sc. In Al–Sc–Zr alloys, however, the Zr concentrations in the precipitates are found to be much lower than their solubility as a result of the small diffusivity of Zr in Al. Fuller et al. studied Al–Sc–Zr alloys at an aging temperature of 300 °C and found that the maximum concentration achieved in the precipitates was only ~ 1.5 at.% Zr, which corresponds to the composition $\text{Al}_3(\text{Sc}_{0.94}\text{Zr}_{0.06})$. Even at higher aging temperatures, very little Zr is incorporated in the precipitates, as shown by a recent three-dimensional atom-probe (3DAP) tomographic study [15]: when aged at 475 °C, the concentration of Zr in the precipitates of an Al–0.09at.%Sc–0.02at.%Zr alloy reached 4.5 at.%. Most of this Zr, however, was at or near the interfacial region. Nevertheless, Al–Sc–Zr alloys exhibit improved precipitate stability and coarsening resistance at 300 °C as a result of the partitioning of Zr to the precipitates and the segregation of Zr at the $\alpha\text{-Al}/\text{Al}_3\text{Sc}$ heterophase interface, where Zr may act as a barrier for the diffusion of Sc across the interface. Zirconium also decreases the lattice parameter of the $\text{Al}_3(\text{Sc}_{1-x}\text{Zr}_x)$ phase [4], thus decreasing the lattice parameter mismatch with the $\alpha\text{-Al}$ matrix. For the same precipitate radius and volume fraction, there was, however, a modest reduction in creep resistance for the Al–Sc–Zr alloys as compared to Al–Sc alloys, as a result of the smaller lattice parameter mismatch, which decreases dislocation-precipitate elastic interactions [11].

Titanium is of interest as a ternary alloying element in creep-resistant Al–Sc alloys, since Ti has the same high solubility in Al_3Sc (L_{12}) as Zr (up to 50% of the Sc can be replaced in the bulk intermetallic) and Ti reduces the lattice parameter of the $\text{Al}_3(\text{Sc}_{1-x}\text{Ti}_x)$ phase to an even greater extent than does Zr [4]. The resulting concomitant reduction in interfacial and elastic strain energies may further improve the coarsening resistance of the $\text{Al}_3(\text{Sc}_{1-x}\text{Ti}_x)$ precipitates, thus resulting in coarse-grained Al–Sc–Ti alloys, which are creep-resistant at temperatures in excess of 300 °C. Additionally, the tracer diffusivity of Ti in Al is much smaller than that for Zr in Al (by a factor of 23 at 300 °C and 14 at 400 °C [16]), which may further reduce the precipitate coarsening kinetics as compared to Al–Sc–Zr alloys. Indeed, in a resistivity study of rapidly-solidified hypereutectic Al–Sc alloys containing 0.36 at.% Sc and Ti concentrations of 0.06 or 0.17 at.%, it was found that the addition of Ti stabilizes the precipitate structure at 300 °C [17]. In quenched hypereutectic Al–0.30at.%Sc–0.12at.%Ti

alloys, micron-size primary particles formed in the liquid state were found to exhibit the L_{12} structure with a Ti-rich composition, $\text{Al}_3(\text{Sc}_{0.33}\text{Ti}_{0.67})$ [18]. To the best of our knowledge, there are no other studies of Al–Sc–Ti alloys.

In the present study, we examine the temporal evolution of size and composition at elevated temperatures of nanosize $\text{Al}_3(\text{Sc}_{1-x}\text{Ti}_x)$ precipitates formed during aging of a dilute, hypoeutectic Al–Sc–Ti alloy. We also measure the effect of these precipitates on hardness at ambient temperature and creep resistance at 300 °C, and compare our results with prior studies on coarse-grained, creep-resistant binary Al–Sc alloys [5,10,12], as well as ternary Al–Mg–Sc [13,19] and Al–Sc–Zr alloys [11].

2. Experimental methods

An Al–0.06at.%Sc–0.06at.%Ti (Al–0.10wt.%Sc–0.10wt.%Ti) alloy was studied. The composition was chosen to guarantee that this alloy was in the appropriate phase fields during homogenization and subsequent aging treatments, employing a calculated ternary phase diagram [20]. The alloy was produced by dilution casting, using Al–1.2at.%Sc and Al–2.26at.%Ti master alloys with 99.99 at.% pure Al. The alloys were melted in an alumina crucible in a resistively-heated furnace at 750 °C in air. After thoroughly stirring, the melt was cast into a graphite mold resting on a large copper platen. Homogenization was performed at 640 °C for 24 h in air, after which the alloy was water-quenched to room temperature. Subsequent aging was performed in air at various temperatures between 300 and 450 °C, and was terminated by water quenching.

Transmission electron microscope (TEM) foils were mechanically ground to a thickness of 200 μm and subsequently electropolished in a solution of 5 vol.% perchloric acid in methanol at -20 °C, which was cooled in a bath of dry ice in methanol. 3DAP tomograph sample blanks were produced by mechanically grinding material to a square cross-section of ca. $200 \times 200 \mu\text{m}^2$. The samples were then electropolished using a two-stage procedure. The initial polishing was performed using a solution of 10 vol.% perchloric acid in acetic acid. The final polishing was performed using a solution of 2 vol.% perchloric acid in butoxyethanol. Proximity histogram plots (proxigrams) [21] were calculated employing *ADAM* [22] using an isoconcentration surface of 9 at.% Sc. Three to four precipitates were analyzed for each aging time. The average precipitate and matrix concentrations were calculated by employing the fraction of total atoms in the relevant volume.

Vickers microhardness measurements were performed with a 200 g weight at room temperature on samples ground to a 1 μm surface finish. Twenty

measurements were recorded on each sample. Compression creep samples were machined into cylinders with an 8 mm diameter and a 16 mm length. Prior to testing, the samples were re-homogenized and aged to produce specimens with precipitates of specific radii, as measured by TEM, shown in Table 1. The samples were tested at 300 °C after a soak at the test temperature for 2 h, to ensure a stable and uniform sample temperature. Tests were performed in a nickel-based superalloy compression cage with boron nitride lubricated platens to reduce the effects of friction. The platen displacement was measured using a linear variable differential transducer, which was connected to an extensometer. Increasing loads were applied to each sample and, for each load, sufficient time was allowed for a minimum strain rate to be established. Tests were terminated when the sample reached 5% strain.

3. Results

3.1. Microstructure and hardness

Fig. 1 shows the evolution of microhardness with aging time at 300 °C for the Al–0.06Sc–0.06Ti alloy (all compositions are given in at.% in what follows), which is typical of classical precipitation hardening behavior: (1) an incubation period; (2) under aging (precipitate formation stage); (3) peak aging; and (4) over-aging (due to coarsening). Comparison with data for the binary Al–0.06Sc alloys (Fig. 2) demonstrates that the addition of 0.06 at.% Ti produces only a relatively modest increase (~ 75 MPa) in the peak hardness at 300 °C. By contrast, addition of 0.06 at.% Sc (resulting in the binary Al–0.12Sc alloy) increases the peak hardness by 300 MPa, demonstrating that Sc is significantly more effective than Ti at increasing strength, with the addition of a given atomic fraction, for the aging temperature of 300 °C. Furthermore, it is apparent that the addition of only 0.005 at.% Zr increases the hardness by 220 MPa with respect to the binary Al–0.06Sc alloy. Zirconium thus also appears to be a more efficient

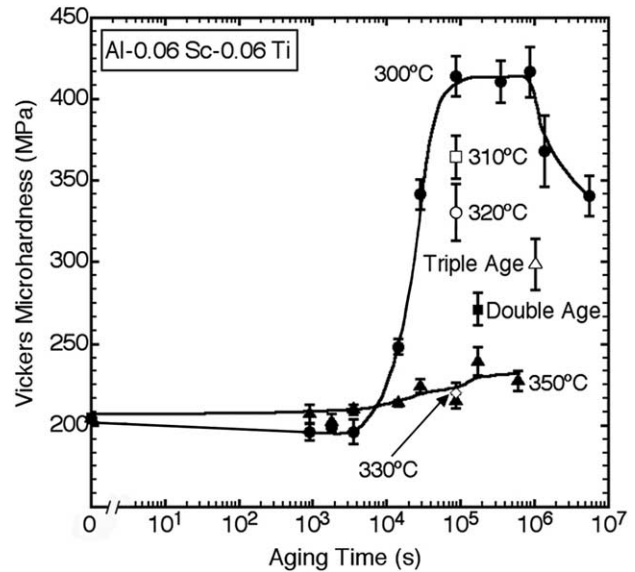


Fig. 1. Microhardness of Al–0.06Sc–0.06Ti vs. aging time for temperatures between 300 and 450 °C. The time for the samples aged at multiple temperatures is the sum of the aging times.

strengthening agent than Ti when aging at 300 °C. Aging at slightly higher temperatures (310 and 320 °C) reduces significantly, however, the peak hardness of Al–0.06Sc–0.06Ti (Fig. 1). Increasing the aging temperature even further to 330 and 350 °C leads to a complete loss of hardening from the precipitates (Fig. 1), which is indicative of very rapid coarsening rates.

A high number density of $\text{Al}_3(\text{Sc}_{1-x}\text{Ti}_x)$ precipitates ($(3 \pm 2) \times 10^{21} \text{ m}^{-3}$) is observed upon peak aging for 24 h at 300 °C. The precipitates remain coherent in the temperature range 300–320 °C, as ascertained by the presence, in two-beam bright-field TEM images, of Ashby–Brown strain contrast [23] typical of coherent precipitates, which is illustrated in Fig. 3 for a sample aged at 320 °C for 24 h. The coherency and nanometer scale of the precipitates is consistent with previous studies on Al–Sc binary alloys [3,5,6] and Al–Mg–Sc and Al–Sc–Zr ternary alloys. Upon aging at 300 °C for up to 64 days, the precipitates remain spheroidal, coherent and

Table 1

Effect of aging treatment (time and temperature) upon average precipitate radius, $\langle R \rangle$, edge-to-edge inter-precipitate spacing, λ , calculated Orowan stress, $\Delta\sigma_{\text{or}}$, and experimental threshold stress, σ_{th} , for Al–0.06Sc–0.06Ti

Aging treatment	Precipitate radius, $\langle R \rangle$ (nm)	Inter-precipitate spacing, λ (nm)	Orowan stress, $\Delta\sigma_{\text{or}}$ (MPa)	Threshold stress, σ_{th} (MPa)
24 h at 300 °C	5.1 ± 0.4	–	–	–
96 h at 300 °C	5.3 ± 0.4	–	–	–
16 day at 300 °C	$5.8 \pm 0.5^{\text{a}}$	141 ± 12	74 ± 5	16 ± 0.2
64 day at 300 °C	7.9 ± 0.7	–	–	–
24 h at 310 °C	$7.4 \pm 0.7^{\text{a}}$	180 ± 17	62 ± 5	17 ± 0.2
24 h at 320 °C	$10.8 \pm 0.9^{\text{a}}$	263 ± 21	47 ± 3	19 ± 0.2
24 h at 300 °C + 48 h at 425 °C	$16.9 \pm 0.8^{\text{a}}$	412 ± 19	33 ± 2	16 ± 0.1
24 h at 300 °C + 240 h at 400 °C + 48 h at 450 °C	10.0 ± 0.8	–	–	–

^a Samples were creep-tested.

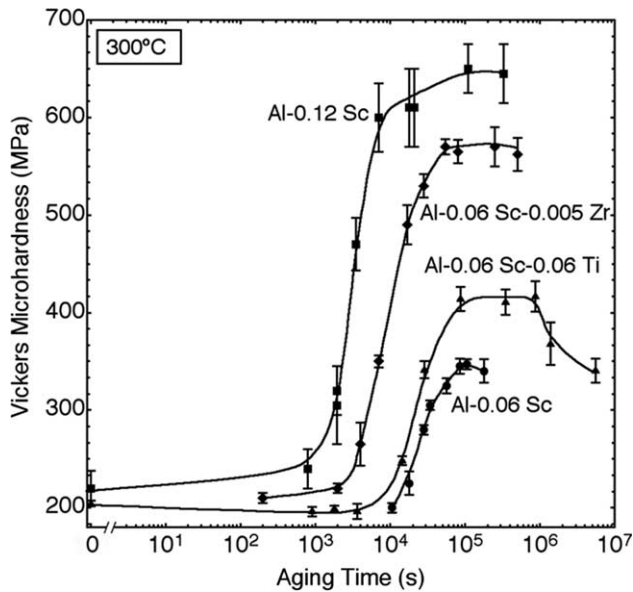


Fig. 2. Microhardness vs. aging time at 300 °C, comparing the present Al–Sc–Ti alloy with binary Al–Sc alloys [5,13], and a ternary Al–Sc–Zr alloy [25].

uniformly distributed in the matrix (Fig. 4(a)). The average radius of the precipitates, $\langle R \rangle$, grows slowly from a value of 5.1 ± 0.4 nm after only 24 h to 7.9 ± 0.7 nm after 64 days of aging, which is a 55% increase in $\langle R \rangle$.

The morphology of the precipitates changes significantly with small changes in aging temperature. When the aging temperature is raised by 20 °C to 320 °C, the precipitates are still distributed homogeneously in the matrix, but they are slightly non-spheroidal and exhibit lobes, which is a sign of growth instabilities (Fig. 4(b)) [24]. The approximate mean particle radius (calculated

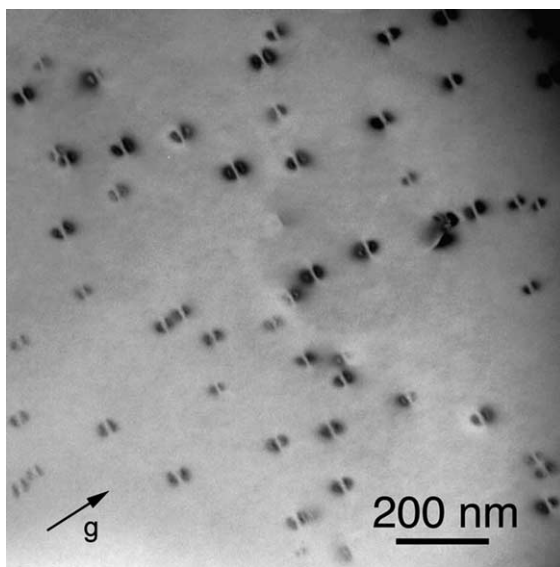


Fig. 3. Two-beam bright-field TEM image showing coherent strain-field contrast around precipitates for Al–0.06Sc–0.06Ti aged at 320 °C for 24 h, $\mathbf{g} = [200]$.

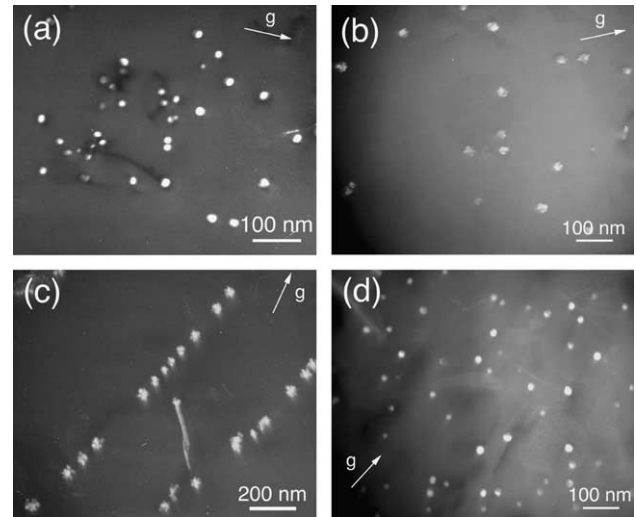


Fig. 4. Dark-field TEM images of Al–0.06Sc–0.06Ti showing changes in precipitate radius, morphology, and distribution with aging treatment: (a) 300 °C for 64 days, [110] projection; (b) 320 °C for 1 day, [100] projection; (c) 330 °C for 1 day, [211] projection; and (d) 300 °C for 1 day, 400 °C for 10 days, and 450 °C for 2 days, [111] projection.

using an area equivalent radius) after a 24 h aging treatment at 320 °C increases to 10.8 ± 0.9 nm, more than double the value at 300 °C. When the aging temperature is raised a mere 10 °C, to 330 °C, the precipitates nucleate predominantly heterogeneously on dislocations (Fig. 4(c)) and exhibit highly non-spheroidal morphologies. The supersaturation decreases with increasing temperature and hence the thermodynamic driving force for nucleation decreases. Precipitation hardening is concomitantly reduced to near zero at and above this aging temperature (Fig. 1).

3.2. Coarsening kinetics and chemical composition

Fig. 5 displays the time dependence of the mean radius, $\langle R \rangle$, at 300 °C for the present Al–0.06Sc–0.06Ti alloy and for a previously studied Al–0.06Sc–0.005Zr alloy [25]. The Lifshitz–Slyozov–Wagner (LSW) coarsening theory [26,27] has been extended to multicomponent alloys by Umantsev and Olson [28], and analyzed in great detail for ternary alloys by Kuehmann and Voorhees, including capillary effects [29]. The time exponent for the evolution of $\langle R \rangle$ of the ternary alloys is predicted to be 1/3, the same as for the binary alloys, albeit with a different rate constant, k , than the LSW model.

$$\langle R(t) \rangle^3 - \langle R(0) \rangle^3 = kt, \quad (1)$$

where t is time.

The $\text{Al}_3(\text{Sc}_{1-x}\text{Ti}_x)$ precipitates were found to coarsen with time exponents smaller than predicted from Eq. (1), as shown in Fig. 5. Assuming the precipitates have reached the quasi-stationary-state coarsening regime after 24 h of aging, the effective time exponent is

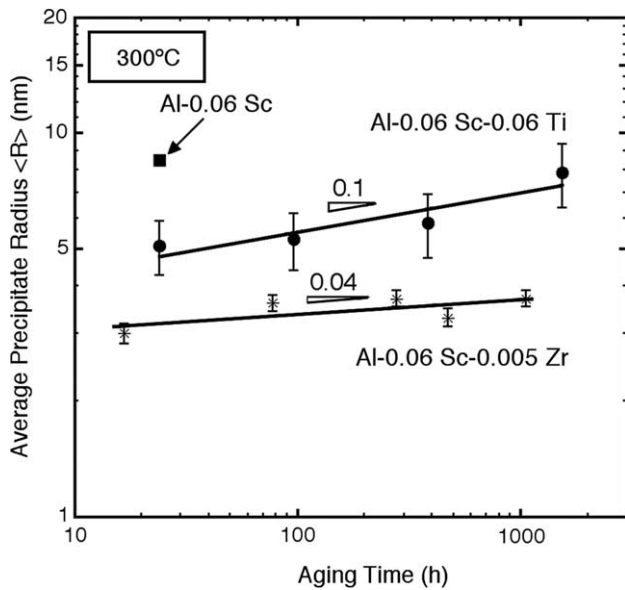


Fig. 5. Double-logarithmic graph of mean precipitate radius, $\langle R \rangle$, for Al-0.06Sc-0.06Ti and Al-0.07Sc-0.005Zr [11] vs. aging time at 300 °C. Both alloys coarsen at a slower rate than predicted by the Kuehmann–Voorhees model for ternary alloys, which predicts a slope of 1/3. One data point for Al-0.06Sc [12] is also shown.

calculated to be ca. 0.1. This is similar to the Al-0.06Sc-0.005Zr alloy, which also coarsens at a slower rate than predicted by the Kuehmann–Voorhees model. The ternary Al-Sc-Ti alloy coarsened at a slower rate than the binary Al-Sc alloy, which was demonstrated to coarsen with a time exponent of ca. 1/3 [5]. The time exponents are, however, difficult to determine accurately in systems in which the precipitates do not coarsen significantly since it is assumed that $R_0 \ll R$; in practice one needs a factor of 10 increase in $\langle R \rangle$ to determine a physically meaningful time exponent. Hence, we refer to them as effective time exponents.

Coarsening resistance is even greater for samples having undergone double or triple aging treatments. Fig. 4(d) exhibits the microstructure of a sample that was subjected to a triple aging treatment: first, aging was performed for 24 h at 300 °C (peak hardness), with the goal of nucleating the precipitates homogeneously; second, aging was performed at 400 °C for 10 days, and thirdly at 450 °C for 48 h, in order to coarsen the precipitates. Despite these very high temperatures, $\langle R \rangle$ remained relatively small at 10.0 ± 0.8 nm (i.e., similar to a single aging for 24 h at 320 °C).

Samples aged for 1, 4, 16 or 64 days at 300 °C were analyzed using 3DAP tomography. The three-dimensional reconstructions demonstrate that $\text{Al}_3(\text{Sc}_{1-x}\text{Ti}_x)$ precipitates with radii corresponding to those measured by TEM are present (Fig. 6). Proxigrams, displaying the concentration of each element as a function of radial distance from the 9 at.% Sc iso-concentration surface, reveal that most of the Sc partitioned to the precipitates with little Sc remaining in the α -Al matrix. Fig. 7 shows

that compared to the matrix, there is an increase in Ti concentration in the precipitates, indicating that Ti also partitions to the precipitates during coarsening and/or during the nucleation and growth stages. The average concentration of Ti in the precipitates continues to increase, albeit slowly, up to the longest aging time analyzed, 64 days.

The concentration of Ti in the precipitates varies with distance from the α -Al/ $\text{Al}_3(\text{Sc}_{1-x}\text{Ti}_x)$ heterophase interface, Fig. 7. At the longer aging times (16 or 64 days), significant Ti segregation occurs at the α -Al/ $\text{Al}_3(\text{Sc}_{1-x}\text{Ti}_x)$ heterophase interface, similar to results found for an Al-0.09Sc-0.05Zr alloy aged for 2412 h at 300 °C. At the shorter aging times (24 or 96 h), no segregation of Ti to this interface is observed at 300 °C, within experimental error.

3.3. Creep properties

Fig. 8 shows the minimum creep rate at 300 °C as a function of the applied compressive stress for four

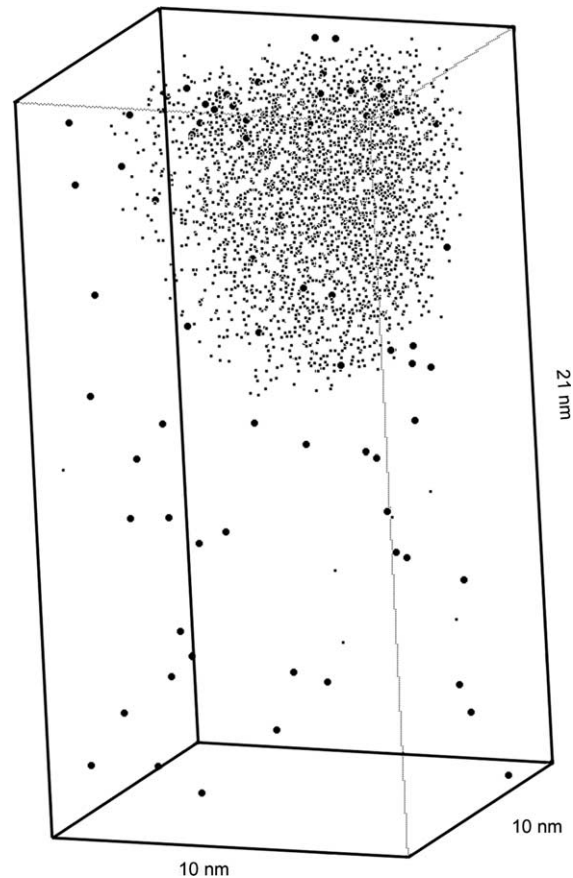


Fig. 6. Three-dimensional reconstruction of a $10 \times 10 \times 21$ nm³ volume analyzed by 3DAP tomography of Al-0.06Sc-0.06Ti aged at 300 °C for 96 h. The small dots represent Sc atoms (which are heavily partitioned to an $\text{Al}_3(\text{Sc}_{1-x}\text{Ti}_x)$ precipitate with L1_2 structure in the upper part of the volume) and the larger spheres represent Ti atoms. For the sake of clarity Al atoms are not included.

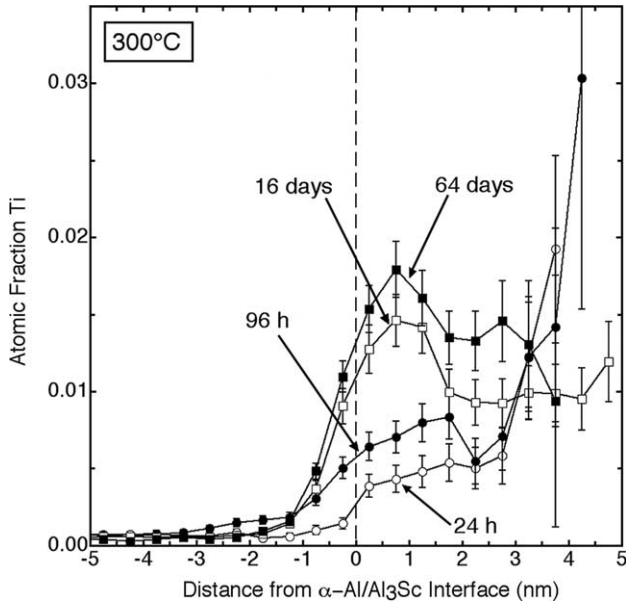


Fig. 7. Proxigram showing the average concentration of Ti in Al-0.06Sc-0.06Ti for various aging times at 300 °C vs. distance from the α -Al/Al₃Sc heterophase interface ($x = 0$), as defined by a 9 at.% Sc isoconcentration surface.

specimens with various precipitate radii (marked with superscript ‘a’ in Table 1). It is apparent that the creep behavior at 300 °C is characterized by high apparent stress exponents, 22–33, indicative of the presence of a threshold stress, σ_{th} , below which the creep rate, $\dot{\epsilon}$, cannot be experimentally measured. The power-law creep equation is then modified as

$$\dot{\epsilon} = A(\sigma - \sigma_{th})^n \exp\left(-\frac{Q}{RT}\right), \quad (2)$$

where A is the Dorn constant, σ is the applied stress, σ_{th} is the threshold stress, Q is the creep activation energy of Al, n is the stress exponent of Al, and R is the ideal gas constant.

Values for the threshold stresses were found according to Eq. (2), by plotting $\dot{\epsilon}^{1/n}$ vs. σ [30] with $n = 4.4$, the stress exponent for pure Al [31]. For smaller precipitate radii, the threshold stresses, and thus the creep resistance, increase with increasing $\langle R \rangle$ (from 16 MPa for the smallest $\langle R \rangle$ of 5.8 nm to 19 MPa for $\langle R \rangle$ equal to 10.8 nm). It then decreases to 16 MPa for the largest $\langle R \rangle$ of 16.9 nm. Due to the high apparent stress exponent, a small relative increase of 3 MPa in threshold stress translates to a large difference in creep rate (in excess of a factor 10) at a given stress. A similar trend (increase followed by decrease of the threshold stresses with increasing $\langle R \rangle$) was also observed in binary Al-Sc [12], as well as in ternary Al-Mg-Sc [13], and Al-Sc-Zr alloys [11]. In these alloys, it is also noted that an increase in volume fraction increases the creep resistance.

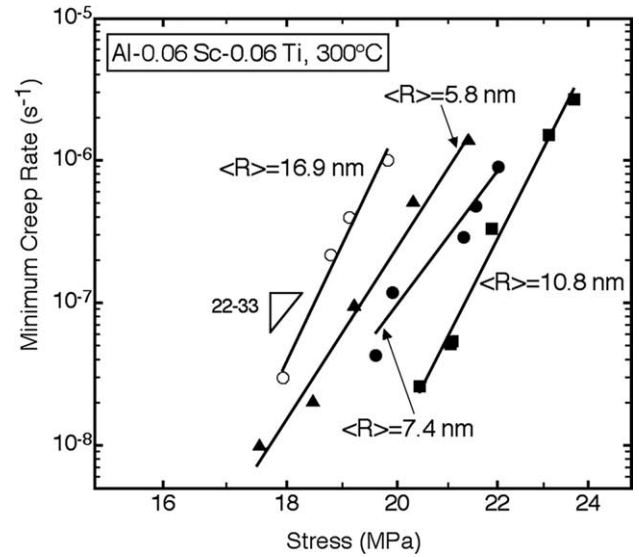


Fig. 8. Double-logarithmic graph of minimum creep strain rate at 300 °C vs. compressive stress for Al-0.06Sc-0.06Ti aged to produce various precipitate radii (given in graph). The stress exponent range is 22–33.

4. Discussion

4.1. Hardness at ambient temperature

The 3DAP tomographic results provide one explanation for the increased hardness of the present Al-0.06Sc-0.06Ti alloy, as compared to the binary Al-0.06Sc alloy (Fig. 2). After peak aging (24 h), the average Ti concentration is much greater in the precipitates (0.50 at.%) than in the matrix (0.076 at.%) yielding a partitioning ratio of $\kappa(\text{Ti}) = 6.6$, defined as the concentration of Ti in the precipitates divided by the concentration of Ti in the matrix. At longer aging times, the concentration of Ti in the precipitates is even greater, with partitioning ratios of up to 40. The incorporation of Ti in the precipitates leads to an increased volume fraction of precipitates. The volume fraction of precipitates is 0.24% after 64 days of aging if Sc but no Ti were to precipitate, as calculated from the matrix Sc concentration of 0.004 at.% measured by 3DAP tomography. For this same aging treatment, the Ti concentration in the precipitates reaches 1.5 at.%, which corresponds to a 6% relative increase in precipitate volume fraction, i.e. from 0.24 to 0.254 vol.%. For aging times longer than 250 h, however, the alloy hardness decreases as precipitate coarsening more than compensates for the increase in volume fraction due to ongoing incorporation of Ti in the precipitates, Fig. 7.

The rapid decrease in peak-hardness with increasing aging temperature indicates that hardness is controlled by $\langle R \rangle$ when all Sc has precipitated out of solution, rather than by a change of precipitate bypass mechanism from shearing to dislocation looping according to

the Orowan mechanism, as in Al–Cu alloys. This hypothesis is tested by calculating the Orowan bypass stress $\Delta\sigma_{\text{or}}$ from [32]

$$\Delta\sigma_{\text{or}} = M \frac{0.4Gb}{\pi\lambda} \frac{\ln(2\bar{r}/b)}{\sqrt{1-\nu}}, \quad (3)$$

where $M = 3.06$ is the orientation factor for aluminum [33], $G = 24.5$ GPa is the shear modulus of aluminum, $\nu = 0.345$ is the Poisson ratio of aluminum, $b = 0.286$ nm is the magnitude of the Burgers vector in aluminum, and λ is the interprecipitate distance given by [34]

$$\lambda = \left[\left(\frac{\pi}{f} \right)^{\frac{1}{2}} - 2 \right] \bar{r}, \quad (4)$$

where f is the volume fraction of precipitates, and $\bar{r} = \sqrt{2/3} \cdot \langle R \rangle$ [32].

Fig. 9 shows the effect of $\langle R \rangle$ on the alloy yield stress increment (as compared to the value for the solutionized, unaged specimen), using a conversion factor of 3 between hardness and strength [35]. For the $\langle R \rangle$ values measured for Al–0.06Sc–0.06Ti ($\langle R \rangle$ equal to 5.1–16.9 nm), the experimental data are in good agreement with predictions from Eq. (3), assuming an Orowan dislocation looping mechanism. Calculations for the shearing mechanisms (using the same equations as in [11]) predict much higher stresses than those given by Eq. (3) over the $\langle R \rangle$ range of interest, confirming that shearing is not operative. These conclusions are in agreement with prior results on Al–0.18Sc [12] and several Al–Sc–Zr alloys [11], for which Orowan dislocation looping was the main strengthening mechanism for $\langle R \rangle$ greater than ~ 2 nm. Furthermore, Miura [36] showed that for deformation at temperatures up to 250 °C, the main mechanism was Orowan dislocation looping or dislocation climb in an Al–0.14Sc alloy, for $\langle R \rangle$ equal to 8 nm. Fig. 9 thus demonstrates the importance of decreasing the coarsening rate of the precipitates by alloying with Ti or Zr, in order to maintain the highest possible strength at ambient temperature.

4.2. Precipitate morphology

As the aging temperature is increased, the precipitate morphology changes from spheroidal at 300 °C (Fig. 4(a)) to exhibiting lobes at 320 °C (Fig. 4(b)), to being cauliflower-shaped at 330 °C (Fig. 4(c)) and 350 °C. A similar effect has been previously observed in Al–0.06Sc alloys [5] aged at temperatures as low as 300 °C, and in an Al–8.2Li alloy aged between 285 and 305 °C [37]. Doherty has described certain conditions under which small surface perturbations can become stable during bulk diffusion-controlled growth [24,38]. One condition for dendritic growth is that the number density of precipitates must be sufficiently low

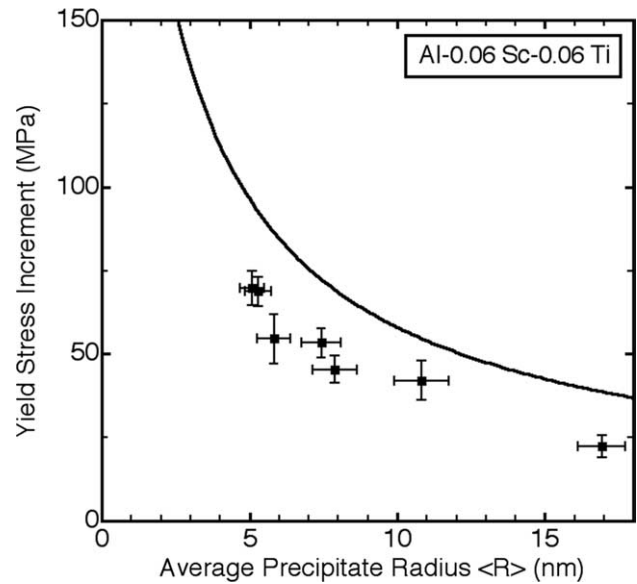


Fig. 9. Yield stress increment (calculated from hardness measurements) vs. mean precipitate radius, $\langle R \rangle$, for Al–0.06Sc–0.06Ti. The solid line is calculated from Eq. (3) for the Orowan dislocation by-pass mechanism.

that the precipitates can grow before their diffusion fields overlap. Thus, diffusion controls growth conditions rather than global equilibrium between the two phase fields. A second condition that promotes dendritic growth is the lack of rapid diffusion paths. Since the interfaces in both the Al–Li and Al–Sc–X alloys are coherent, rapid (short-circuit) diffusion along the interface is not anticipated. Also, since the precipitates are ordered, a more rapid diffusion in the precipitate, compared with the matrix is not expected, since in general diffusivities in ordered phases are smaller than in disordered solid-solutions [39]. Furthermore, the Al_3Sc phase exhibits a much higher melting temperature than the $\alpha\text{-Al}$ matrix (1320 and 660 °C, respectively), further increasing the diffusivity difference between these two phases with very different homologous temperatures.

4.3. Coarsening kinetics

Equilibrium was not achieved in the present Al–Sc–Ti alloy, as illustrated by the fact that the concentration of Ti in the precipitates increases continuously to the longest aging time studied, 64 days (Fig. 10). The average Sc/Ti (at.%/at.%) ratio in the precipitates decreases from 65 to 19 for the range of aging times studied, which is considerably greater than the achievable value of unity [4]. In the matrix, the Ti concentration decreases from 0.07 to 0.04 at.% (Fig. 11) and has thus not yet reached the calculated equilibrium value of 0.01 at.% [20].

It is apparent from Fig. 5 that Ti has the effect of retarding significantly the coarsening kinetics as compared to Al–0.06Sc (e.g., the precipitates reach the same

mean radius after aging for 1 day in the binary alloy and 64 days in the ternary alloy). This is in agreement with previous studies of Al–Sc–Zr alloys, where the addition of Zr also retards the coarsening kinetics, as illustrated in Fig. 5 for Al–0.06Sc–0.005Zr. As noted in Section 1, it was suggested by Fuller et al. that Zr segregates at the heterophase interface, which may act as a barrier to diffusion. Titanium also reduces the coarsening kinetics, as indicated by the small values of the effective time exponent (0.1 for Ti and 0.04–0.05 for Zr, Fig. 5). One possible explanation for the lack of agreement with the Kuehmann–Voorhees coarsening model is that these systems have not yet entered the quasi-steady-state coarsening regime, since the compositions of both the matrix and precipitates are continuously changing significantly up to the longest aging times studied (Figs. 10 and 11). Thus, (dC/dt) is not approximately equal to zero, which is an assumption of the KV model for a ternary alloy. Other possible reasons are that the KV model neglects the off-diagonal terms in the diffusion tensor and also assumes that the chemical potential of the vacancy is everywhere equal to zero.

The effect of the reduced coarsening rate is even more apparent in Al–0.06Sc–0.06Ti samples which have undergone double or triple aging, consisting of a first aging treatment at 300 °C followed by one or two treatments at higher temperatures. In Fig. 4(d), it can be seen that $\langle R \rangle$ remains relatively small (10.0 ± 1.6 nm), even after aging at a temperature of 450 °C, resulting in the retention of hardness, Fig. 1. By contrast, aging for one day at 330 °C leads to a complete loss of hardness,

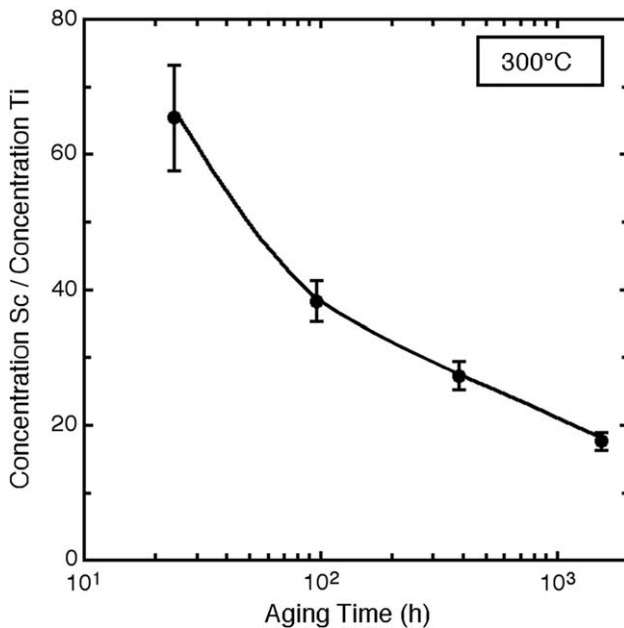


Fig. 10. Ratio of the average concentration of Sc (at.%) to Ti (at.%) in precipitates in Al–0.06Sc–0.06Ti as measured by 3DAP tomography vs. aging time at 300 °C.

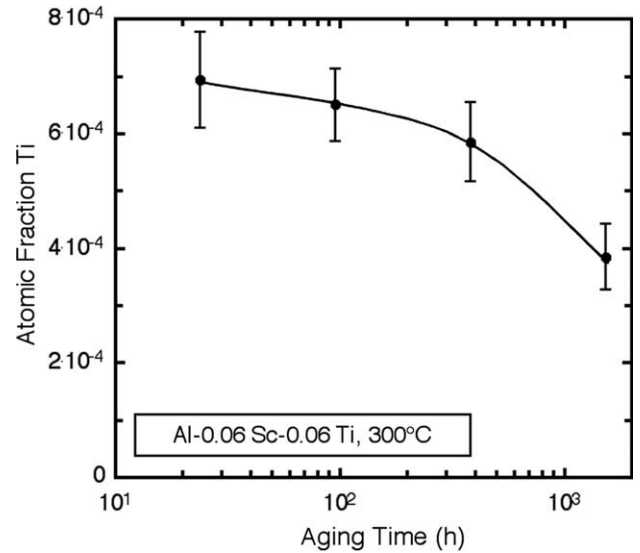


Fig. 11. Ti matrix concentration in Al–0.06Sc–0.06Ti vs. aging time at 300 °C.

and thus much larger precipitate sizes, on the order of 50 nm across the non-spheroidal precipitates. It appears that once precipitates have nucleated, they are resistant to coarsening. It remains to be determined if the Ti concentration in the precipitates plays a significant role in this effect.

In the Al–Sc–Ti system, the interface dominates the coarsening process since the parameter $L = \varepsilon^2 C_{44} / \gamma$ is ca. 5×10^{-2} (where $\varepsilon = 0.009$ is the constrained lattice parameter misfit, $l = 5\text{--}10$ nm is a characteristic length taken as the precipitate radius, $C_{44} = 25.4$ GPa [31] is an elastic constant of the matrix and $\gamma = 160\text{--}185$ mJ m⁻² [40] is the interfacial energy), which is much less than the critical value of ca. 5, below which the coarsening rate is not significantly affected by the elastic stresses [41,42]. Since the interfacial energy dominates, a change in the interfacial energy can have a considerable effect on decreasing the coarsening rate, as the coarsening rate constant contains the interfacial free energy in the numerator. The segregation of Ti to the interface thus becomes important, as it can affect the heterophase interfacial energy. The Gibbsian excess of Ti relative to Al and Sc is [43]

$$\Gamma_{\text{Ti}}^{\text{Al,Sc}} = \Gamma_{\text{Ti}} - \Gamma_{\text{Sc}} \left(\frac{C_{\text{Al}}^{\alpha} C_{\text{Ti}}^{\beta} - C_{\text{Al}}^{\beta} C_{\text{Ti}}^{\alpha}}{C_{\text{Al}}^{\alpha} C_{\text{Sc}}^{\beta} - C_{\text{Al}}^{\beta} C_{\text{Sc}}^{\alpha}} \right) - \Gamma_{\text{Al}} \left(\frac{C_{\text{Ti}}^{\alpha} C_{\text{Sc}}^{\beta} - C_{\text{Ti}}^{\beta} C_{\text{Sc}}^{\alpha}}{C_{\text{Al}}^{\alpha} C_{\text{Sc}}^{\beta} - C_{\text{Al}}^{\beta} C_{\text{Sc}}^{\alpha}} \right), \quad (5)$$

where Γ_m is the Gibbsian interfacial excess of element m and C_m^n is the equilibrium concentration of element m in phase n , where α and β are the precipitate and matrix phases, respectively (Γ_{Ti} is found to be much larger than the other two Γ_m terms in Eq. (5)). Both Γ_m and C_m^n were obtained from the 3DAP tomography proxigrams.

Eq. (5) yields a value of $\Gamma_{\text{Ti}}^{\text{Al,Sc}} = 0.60 \pm 0.38$ atoms nm^{-2} after aging for 1536 h. This is smaller than the Gibbsian excess of Zr relative to Al for an Al–0.09Sc–0.05Zr alloy, where $\Gamma_{\text{Zr}}^{\text{Al,Sc}}$ achieves a value of 1.23 ± 0.62 atoms nm^{-2} after aging for a shorter period (576 h) at the same temperature, 300 °C. This indicates that Ti segregates to a lesser degree than Zr, as expected since Ti is a slower diffuser, ($(D_{\text{Zr}}/D_{\text{Ti}}) = 23$ at 300 °C [16,44]). It could also indicate that more Zr is needed to produce a similar reduction in the lattice parameter misfit, since interfacial segregation could potentially lead to a reduction in the strain energy as the presence of additional Ti at the interface will reduce the lattice parameter mismatch.

At 300 °C, the segregation of the Ti to the interface could result from the fact that Ti diffuses more slowly in the precipitate phase since it is an ordered intermetallic compound [39]. Hence, the coarsening of the precipitates may be interface-limited, since it diffuses to the precipitate through the matrix at a faster rate than it can be incorporated into the precipitate. Furthermore, interfacial segregation is driven by the reduction in the heterophase interfacial free energy. According to the Gibbs adsorption isotherm for an ideal dilute solution (Eq. (6)), after 64 days of aging the interfacial free energy is reduced by 3.0% for the {100} facets and by 2.6% for the facets, employing values of 160 mJ m^{-2} for {100} facets and 185 mJ m^{-2} for {111} facets [40]

$$\Gamma_{\text{Ti}}^{\text{Al,Sc}} = -\frac{C_{\text{Ti}}}{kT} \left(\frac{\partial \gamma}{\partial C_{\text{Ti}}} \right), \quad (6)$$

where γ is the interfacial free energy, C_{Ti} is the concentration of Ti in the matrix and $\Gamma_{\text{Ti}}^{\text{Al,Sc}}$ is the relative Gibbsian interfacial excess of Ti with respect to Al and Sc.

Despite the similarly small values for the time exponent, the radii of the precipitates in the Al–0.06Sc–0.06Ti alloy are greater than the radii observed in the corresponding Zr-containing alloy, Al–0.06Sc–0.005Zr, for identical aging treatments, Fig. 5. One possible explanation for the differences in $\langle R \rangle$ between the alloys is that the diffusivity of Ti in Al is even slower than that of Zr. Thus, the diffusivities of the Sc and Ti are so disparate (at 300 °C, $D_{\text{Sc}}/D_{\text{Ti}} = 3.3 \times 10^5$ [16,44]) that diffusion of Sc is unhindered by the presence of Ti, which remains mainly in solution until after the Al_3Sc precipitates have nucleated and commenced coarsening. In the case of Al–Sc–Zr, the ratio $D_{\text{Sc}}/D_{\text{Zr}}$ (at 300 °C, $D_{\text{Sc}}/D_{\text{Zr}} = 1.4 \times 10^4$ [44]) is smaller and thus the diffusivities of the Sc and Zr are perhaps close enough that Zr has an effect on the precipitates before they are able to grow to the radii observed in the Al–Sc–Ti system.

The presence of different radii in the two alloys can be used to explain the fact that Ti is not as effective a hardener (strengthenener) at room temperature as Zr. Since Ti is not as effective at preventing the $\text{Al}_3(\text{Sc}_{1-x}\text{Ti}_x)$ precipitates from coarsening in the initial stages, the precipi-

tates are correspondingly larger for comparable alloy compositions and aging treatments, Fig. 5. Since the microhardness is dependent on radius and interprecipitate spacing of the precipitates, the Al–Sc–Zr alloy is correspondingly harder, as illustrated in Fig. 2.

4.4. Creep properties

A threshold behavior was also found previously in similar coarse-grained Al–Sc [10,12], Al–Mg–Sc [13] and Al–Sc–Zr [11] alloys with nanosize Al_3Sc (L_{12}) precipitates. A similar behavior was also observed in Al–Zr–V alloys with L_{12} precipitates [45]. In these articles it is shown that the threshold stress originates from the interaction of dislocations with precipitates. The first possible mechanism, precipitate shearing, predicts threshold stress values much greater than measured experimentally, and can thus be discarded, similar to precipitate shearing at ambient temperature. The second possible mechanism, dislocation-bypass by climb of coherent precipitates, predicts threshold values that are smaller than those measured and are independent of radius [46,47]. This discrepancy was resolved by considering additional elastic interactions between the bypassing dislocations and the precipitates, whose origins are the lattice parameter and stiffness mismatches between coherent precipitates and matrix [48]. An important prediction of this modified climb model is that the threshold stress normalized by the Orowan stress should increase with increasing $\langle R \rangle$ to values as large as 0.5, whereas the original climb model predicts a small value (less than 0.05), which is independent of $\langle R \rangle$. Prior data on Al–Sc [10,12], Al–Mg–Sc [13] and Al–Sc–Zr [11] alloys does indeed agree semi-quantitatively with these predictions.

Plotting the threshold stress results for Al–0.06Sc–0.06Ti in a normalized threshold stress plot (Fig. 12), it is apparent that the general trend is very similar to that found for previously studied Al–Sc, Al–Mg–Sc and Al–Sc–Zr alloys, and in semi-quantitative agreement with model predictions [48]. The use of the normalized threshold stress removes the dependency on precipitate volume fraction, and thus allows for direct comparison of alloys with different volume fractions of precipitates. A slight decrease in normalized threshold stress is apparent for both Al–Sc–Zr and Al–Sc–Ti alloys, as compared to Al–Sc and Al–Mg–Sc alloys. This is expected qualitatively due to the reduced lattice parameters of $\text{Al}_3(\text{Sc,Zr})$ and $\text{Al}_3(\text{Sc,Ti})$ as compared to Al_3Sc , which leads to a reduction in lattice parameter mismatch between the precipitates and the matrix. This effect results in a reduction of elastic interactions between lattice dislocations and the precipitates they bypass by climb, and a concomitant decrease in threshold stress. For a Ti precipitate concentration of 1.5 at.% at 300 °C, the lattice mismatch is reduced by a small amount, i.e., from 1.10% to 1.08% [4,49]. The

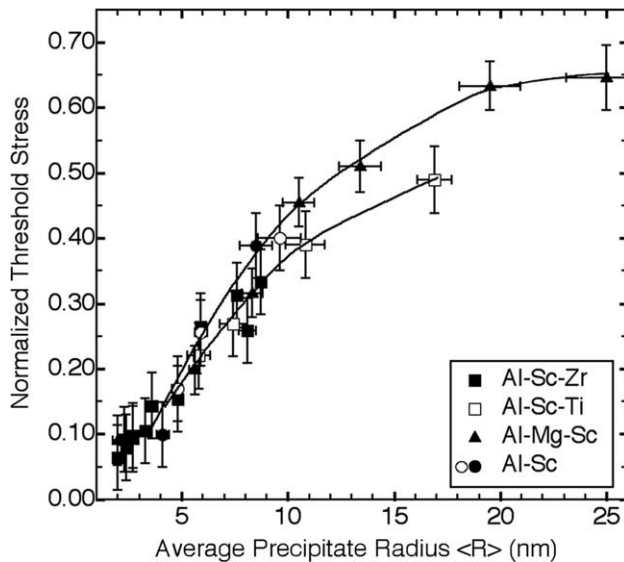


Fig. 12. Measured creep threshold stress at 300 °C normalized by calculated Orowan stress at 300 °C vs. mean precipitate radius, $\langle R \rangle$, for Al–0.06Sc–0.06Ti and for binary Al–Sc alloys [12] and ternary Al–Sc–Zr alloys [11].

difference between the binary and the ternary alloys is more apparent at larger radii since the elastic interaction volume of the precipitate scales with $\langle R \rangle^3$. The lack of a decrease in normalized threshold stress for the Al–Sc–Mg alloys may be due to the fact that Mg does not affect the near-threshold creep behavior.

In summary, the addition of Ti to binary Al–Sc alloys decreases slightly the creep resistance for given values of precipitate volume fraction and $\langle R \rangle$, as shown by the decreased normalized threshold stress values, Fig. 12. The coarsening resistance of the precipitates is, however, much improved, Fig. 5, so that the overall long-term creep resistance at 300 °C is expected to be improved. The excellent coarsening resistance observed in the alloys subjected to triple coarsening may make long-term use of Al–Sc–Ti at ca. 350 °C possible. At this temperature, binary Al–Sc alloys coarsen very rapidly [5] and are expected to exhibit almost no threshold stress. They therefore display very poor creep resistance at these temperatures. As compared to Al–Sc–Zr alloys, Al–Sc–Ti alloys have similar creep and coarsening properties. Although Ti is less expensive than Zr, the benefits of replacing Zr with Ti as a ternary alloying element in Al–Sc alloys are uncertain.

5. Conclusions

The nanostructure and mechanical properties of an Al–0.06Sc–0.06Ti alloy were examined at aging temperatures between 300 and 450 °C for up to 64 days (1536 h), leading to the following conclusions:

- Spheroidal, coherent $\text{Al}_3(\text{Sc}_{1-x}\text{Ti}_x)$ precipitates with $L1_2$ structure are formed upon aging at 300 °C, leading to peak hardness after 24 h, which is higher than for Al–0.06Sc, but lower than for Al–0.12Sc or Al–0.06Sc–0.005Zr. Increasing the aging temperature to 320 °C reduces peak hardness and the precipitates exhibit lobes and cusps due to the smaller Ti supersaturation. At 330 °C, precipitation occurs mostly heterogeneously on dislocations and precipitation hardening is lost.
- At 300 °C, the precipitates coarsen at a significantly slower rate than observed in binary Al–Sc alloys or predicted by the Kuehmann–Voorhees coarsening model for a ternary alloy. This is due to incorporation of Ti in the precipitates, which also explains the increased hardness at ambient temperature as compared to the binary alloy. Titanium is, however, not as effective as Zr at reducing precipitate coarsening and hardening the Al–Sc alloy.
- At 300 °C, Ti partitions to the $\text{Al}_3(\text{Sc}_{1-x}\text{Ti}_x)$ precipitates, although most of the Ti remains in solid-solution in the matrix ($x = 0.06$ for the longest aging time analyzed, 64 days). The concentration in the matrix and the precipitates continues to change up to the longest aging time analyzed, indicating that global thermodynamic equilibrium is not achieved. The much slower diffusion of Ti as compared to Sc most likely explains why precipitate coarsening occurs more slowly than in the binary Al–Sc alloy.
- For the specimens analyzed employing a 3DAP tomograph, after aging for longer periods at 300 °C (16 or 64 days), Ti segregates to the $\alpha\text{-Al}/\text{Al}_3(\text{Sc}_{1-x}\text{Ti}_x)$ heterophase interface, as reported previously for Zr in Al–Sc–Zr alloys. Segregation is not found for shorter aging times, 1 or 4 days.
- A creep threshold stress is found at 300 °C, which when normalized by the Orowan stress, increases with increasing precipitate radius, $\langle R \rangle$, similarly to the previously studied alloys, Al–Sc, Al–Mg–Sc and Al–Sc–Zr. This is in semi-quantitative agreement with predictions from a model considering dislocation climb bypass including elastic interactions with the misfitting precipitates.

Acknowledgments

This research is supported by the US Department of Energy through grant DE-FG02-98ER45721. The authors thank Ashurst Inc. for supplying the Al–Sc master alloy, Alcoa Inc. for supplying the Al–Ti master alloy, and Dr. Joanne Murray from Alcoa Inc. for the calculated ternary Al–Sc–Ti phase diagram.

References

- [1] Royset J, Ryum N. *Int Mater Rev* 2005;50(2):1–26.
- [2] Hyland RW. *Metall Trans A* 1992;23A:1947–55.
- [3] Novotny GM, Ardell AJ. *Mater Sci Eng A* 2001;A318:144–54.
- [4] Harada Y, Dunand DC. *Mater Sci Eng A* 2002;329–331: 686–695.
- [5] Marquis EA, Seidman DN. *Acta Mater* 2001;49:1909–19.
- [6] Iwamura S, Miura Y. *Acta Mater* 2004;52:591–600.
- [7] Kendig K, Miracle D. *Acta Mater* 2002;50:4165–75.
- [8] Toropova LS, Eskin DG, Kharakterova ML, Dobatkina TV. *Advanced Aluminum Alloys Containing Scandium*. Reading: Gordon & Breach; 1998.
- [9] Sawtell RR, Jensen CJ. *Metall Trans A* 1990;21A:421–30.
- [10] Fuller CB, Seidman DN, Dunand DC. *Scripta Mater* 1999;40: 691–6.
- [11] Fuller CB, Seidman DN, Dunand DC. *Acta Mater* 2003;51: 4803–14.
- [12] Marquis EA, Seidman DN, Dunand DC. *Acta Mater* 2002;50: 4021–35.
- [13] Marquis EA, Seidman DN, Dunand DC. *Acta Mater* 2003;51: 4751–60.
- [14] Clouet E. Ph.D. Thesis, Ecole Centrale Paris, 2004.
- [15] Forbord B, Lefebvre W, Danoix F, Hallem H, Marthinsen K. *Scripta Mater* 2004;51:333–7.
- [16] Bergner D, Chi NV. *Wissenschaftliche Zeitschrift der Pädagogischen Hochschule "N.K. Krupskaja", Halle XV, Heft 3, 1977*.
- [17] Schmidt U, Beresina AL, Chuistov KV, Monastyrskaja TA, Rud AD. *Decomposition of rapidly quenched supersaturated Al–Sc–X (X:Li, Ta, Ti) alloys*. In: *Advanced light alloys and composites*. Dordrecht: Kluwer Academic Publishers; 1998.
- [18] Hyde KBNA, Prangnell PB. *Mater Sci For* 2002;396(4):39–44.
- [19] Marquis EA, Seidman DN, Asta M, Woodward C, Ozolins V. *Phys Rev B* 2003;92:36101-1–3.
- [20] Murray JL. Personal communication, 2003.
- [21] Hellman OC, Vandenbroucke JA, Rüsing J, Isheim D, Seidman DN. *Microsc Microanal* 2000;6:437–44.
- [22] Hellman OC, Vandenbroucke J, du Rivage JB, Seidman DN. *Mater Sci Eng A* 2002;327(1):29–33.
- [23] Ashby M, Brown L. *Philos Mag* 1963;8:1083–102.
- [24] Doherty RD. *Metal Sci* 1982;16:1–13.
- [25] Fuller CB. Ph.D. Thesis, Northwestern University, 2003.
- [26] Lifshitz IM, Slyozov VV. *J Phys Chem Solids* 1961;19:35–50.
- [27] Wagner C. *Z Elektrochem* 1961;65:581–91.
- [28] Umantsev A, Olson GB. *Scripta Metall Mater* 1993;29:1135–40.
- [29] Kuehmann CJ, Voorhees PW. *Metall Mater Trans A* 1996;27A:937–43.
- [30] Lagneborg R, Bergman B. *Metal Sci* 1976;10:20–8.
- [31] Frost HJ, Ashby MF. *Deformation-mechanism maps: The plasticity and creep of metals and ceramics*. Oxford: Pergamon; 1982.
- [32] Hirsch PB, Humphreys FJ. In: Argon A, editor. *The physics and strength of plasticity*. Cambridge (MA): MIT Press; 1969.
- [33] Martin PW. *Precipitation hardening*. London: Butterworth-Heinemann; 1998.
- [34] Brown LM, Ham RK. *Dislocation–particle interactions*. In: *Strengthening methods in crystals*. App. Sci. Pub.; 1971.
- [35] Tabor D. *Br J App Phys* 1956;7:159–65.
- [36] Miura Y, Nakayama M, Furuta A. *JIMIS-7, 1993*.
- [37] Baumann SF, Williams DB. *Met Trans A* 1985;16A:1203–11.
- [38] Mullins WW, Sekerka RF. *J App Phys* 1963;34(2):323–31.
- [39] Shewmon PG. *Diffusion in solids*. New York: McGraw-Hill; 1963.
- [40] Asta M, Foiles SM, Quong AA. *Phys Rev B* 1998;57:11265–75.
- [41] Thompson ME, Su CS, Voorhees PW. *Acta Metall Mater* 1994;42:2107–22.
- [42] Thornton K, Akaiwa N, Voorhees PW. *Acta Mater* 2004;52:1365–78.
- [43] Dregia SA, Wynblatt P. *Acta Metall Mater* 1991;39(5):771–8.
- [44] Fujikawa SI. *Defect Diffus For* 1997;143–147:115–20.
- [45] Chen YC, Fine ME, Weertman JR. *Acta Metall Mater* 1990;38(5):771–80.
- [46] Arzt E, Rosler J. *Acta Metall* 1988;36(4):1053–60.
- [47] Rosler J, Arzt E. *Acta Metall* 1990;38(4):671–83.
- [48] Marquis EA, Dunand DC. *Scripta Mater* 2002;47:503–8.
- [49] Touloukian YS, Kirby RK, Taylor RE, Desai PD. *Thermophysical properties of high temperature solid materials*. New York: Macmillan; 1967.